Rheological Response of Entangled Isotactic Polypropylene Melts in Strong Shear Flows: Edge Fracture, Flow Curves and Normal Stresses

Daniele Parisi, Aijie Han, Jiho Seo, and Ralph H. Colby*

Materials Science and Engineering, The Pennsylvania State University, University Park, PA 16802

*corresponding author rhc@plmsc.psu.edu

ABSTRACT

Isotactic polypropylene (iPP) melts are industrial semicrystalline polymers whose processing typically involves strong shear flows. The study of the rheological response of iPP melts, well beyond the linear viscoelastic limit, is limited by edge fracture which manifests in rotational rheometers. In this work, we used a reflection polariscope under shear to detect the onset shear rate at which edge fracture is observed, for various rotational rheometry fixture diameters. The onset shear rate for edge fracture was found to correlate with the zero-shear viscosity, enabling the prediction of edge fracture by only knowing the zero-shear viscosity; a quantity which is easier to measure compared to the second normal stress difference. Edge fracture is then mitigated by using a cone-partitioned plate, which enabled the study of the first normal stress difference, and in combination with capillary rheometry, allowed the measurement of flow curves with very well-resolved shear thinning region. For strongly polydisperse iPPs at high shear rates, we found that viscosity scales as the -0.7 power of shear rate, while primary normal stress difference scales as the square root of shear rate. The dependence of the shear thinning of isotactic polypropylenes on polydispersity was then unravelled, offering a broad set of data to develop and test molecular models.

INTRODUCTION

Unit operations in polymer processing such as injection molding and film blowing promote strong flow fields to the processed materials. Isotactic polypropylene (iPP) is a large volume commodity polymer employed in many everyday products. Its simple chemical structure with strictly linear chains and semicrystalline nature, makes it one of the most suitable model systems to investigate flow-induced crystallization (FIC) [1–16].

The study of FIC in a rotational rheometer is complicated because of elastic instabilities which typically manifest at the sample/gas interface as a result of unbalanced forces: the second normal stress difference overcomes the surface tension that keeps stable the rim of the sample during the shear flow [17,18]. This phenomenon is commonly known as edge fracture and is responsible for a strong distortion of the flow field during shear rheological experiments of viscoelastic materials [17,19–21]. Over the years, many contributions have been focusing on the nature of edge fracture and ploys to avoid or at least minimize its effect on the measurement of rheological properties [18,22–25]. Edge fracture materializes in nonlinear shear experiments in both polymer melts and solutions, as well as in pastes and greases [20]. A typical fingerprint of edge fracture manifests in steady-shear experiments as a continuous drop of the shear stress (or shear viscosity) over time, without eventually reaching any steady-state. This is due to a continuous loss of sample from the measuring area. In particular cases, where the shear flow is utilized as a promoting agent for morphological changes in the system, the presence of edge fracture precludes a simple shear flow, a necessary condition to study both FIC and the shear rate dependence of viscosity. Mykhaylyk *et al*. [27] studied how edge fracture perturbs FIC and how this is reflected in the X-ray scattering patterns.

Edge fracture is not easy to predict. Hutton [21], Tanner and Keentok [17] observed that edge fracture occurs when the second normal stress difference (N_2) exceeds a critical value ($N_{2,c}$) which is a function of the surface tension of the fluid and the fracture diameter [17], as well as temperature and shear rate [23]. A simplified relation for $N_{2,c}$ writes [17]:

$$N_{2,c} = \frac{2\Gamma}{3a} \tag{1}$$

where Γ is the surface tension and a is the radius of a semi-circular indentation that occurs during edge fracture (see Figure 1). When a is equal to half of the gap at the perimeter of the plate-plate geometry (or cone-plate), the fracture occupies the full width of the gap at the rim, constituting the extreme case. The estimation of a represents the main challenge in using this approach [17].

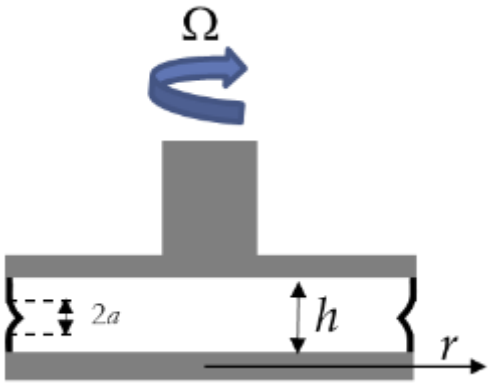

Figure 1. Schematic illustration of the edge fracture phenomenon in a parallel plate geometry. Ω is the angular velocity, *h* is the measuring gap, *r* is radial position of the plate, and *a* is radius of the semi-circular indentation that occurs during edge fracture, according to Tanner and Kentook [17].

A more recent approach proposed by Hemmingway and Fielding [18], expresses the critical conditions for edge fracture as:

$$\sigma \frac{\partial |N_2|}{\partial \sigma} > \frac{4\pi\Gamma}{h} \tag{2}$$

where σ is the shear stress and *h* is the measuring gap. While the shear stress is a directly measured quantity, the measurement of the second normal stress difference in rotational rheometers is nontrivial; it requires special rheometry and analysis [23,25-26,28]. We here suggest the interesting correlation between the onset of edge fracture and the zero-shear viscosity to predict edge fracture, rather than the measurement of the second normal stress difference.

Predicting and minimizing edge fracture is essential for fundamental studies on the shear thinning of polydisperse polymers. There is no universal description leading to scaling laws for shear thinning in polymer solutions and melts. The onset of viscosity thinning occurs when the shear rate ($\dot{\gamma}$) is higher than the inverse of the Rouse time ($1/\tau$) of the longest chains in the system (proven to coincide with the τ from the Cross model fits for iPP1,3,4,5,6 in Ref. [15]). In other words, the thinning happens when a substantial fraction of polymer chains is oriented and stretched in the flow direction [29]. The Doi-Edwards tube model [30] predicts a shear thinning regime with $\eta \sim \dot{\gamma}^{-1.5}$ based on the segmental orientation of the chain in the flow direction, which relaxes on the time scale of the reptation time, along with an instantaneous retraction of the chain inside the deformed tube. However, this prediction yielded an overestimation of the observed shear thinning. Subsequently, the instant retraction of the stretched chain was substituted with a Rouse retraction of the chain at a time scale equal to the Rouse time [31,32]. Such a modification reduced the gap between experiments and predictions, with a power

law shear thinning $\eta \sim \dot{\gamma}^{-m}$ but still, the predicted shear thinning exponent $m > 1$. A significant improvement was obtained by introducing the concept of convective constraint release (CCR) conceived by Marrucci [33] and recently revised by Marrucci and Ianniruberto [34,35]. CCR refers to the mechanism by which entanglements are released as a result of convective flow acting on the chains surrounding a test chain. The CCR model predicted a shear thinning exponent $m < 1$ [36]. However, due to the presence of an adjustable parameter in the CCR model (accounting for the severity of the CCR), a single value of the thinning exponent m does not emerge. Nevertheless, by including CCR in the tube theory for linear entangled polymers, good agreement with experimental results was reported [36]. Experiments on nearly monodisperse entangled polymer melts and solutions reported a shear thinning exponent between 0.8 and 0.9 [22,37,38,39]. However, the effect of the molecular weight distribution on the shear thinning is not thoroughly explored [40,41], in part because of the challenge in obtaining reliable steady shear viscosity data at very high shear rates.

In the present work, six entangled isotactic polypropylene melts with different molecular characteristics were used to investigate edge fracture and shear thinning above the nominal melting temperature (T_m ~ 168 °C). The presence of flow instabilities was first investigated by means of a Shear-Induced Polarized Light Imaging (SIPLI) setup [42,43], to define the limit of shear rates where edge fracture occurs. We find that the critical shear rate for edge fracture correlates with the zero-shear viscosity. Subsequently, the minimization of edge fracture in the measuring area was achieved by using a cone-partitioned plate (CPP) [22,25]. The use of the CPP allowed to measure steady-state viscosity for long times, nearly unaffected by edge fracture. Finally, the combination of different rheological techniques, including the use of the CPP and a capillary rheometer, enabled the creation of flow curves covering six decades in shear rate; from the Newtonian plateau to a very well-resolved power law shear thinning regime. This experimental result is thought to be significant for studying the shear thinning of the steady state viscosity of thermoplastic polymer melts, and to motivate the development of molecular models.

EXPERIMENTAL

Materials. Six commercial linear isotactic polypropylene samples were used. Samples are coded iPP followed by a number from one to six. iPP 1-5 were studied in Refs. [4,5,12], iPP 6 in Ref. [15]. Molecular characteristics and linear viscoelastic properties (at 170 °C) are reported in Table 1 as well as the xylene-soluble fraction (XS), which is indicative of tacticity. The small amplitude oscillatory shear response at 170 °C is reported in Figure S1 in the Supporting Information. Differential scanning calorimetry (DSC) curves and size-exclusion chromatography are discussed elsewhere [4,5,12,15].

Reported values for the equilibrium melting (T_m^0), nominal melting (T_m) and glass transition (T_g) temperatures are 187±2 °C [43], ~168 °C [15], and -35 < T_g < 10°C [44], respectively.

Rheology. Rheological experiments were all performed at 170 °C, slightly above the nominal highest melting temperature (T_m ~ 168 °C) [15]. Samples were subjected to an annealing process at 220 °C for 10 minutes (well above the equilibrium melting temperature ~ 187 °C [44]) prior to any measurements, to partially remove thermal and shear histories [4,15]. The same temperature was used to prepare disks to facilitate the sample loading in the rheometer. Samples were press-molded for twenty minutes in a glove box under nitrogen, into 8 or 25 mm disks with ~ 1 mm thickness. Oxygen-free environment was guaranteed for both sample preparation and rheological tests in order to minimize oxidation.

Table 1. Molecular characteristics and viscoelastic properties of isotactic polypropylene samples

iPP	1	2	3	4	5	6
M_w [kg/mol][a]	440	158	236	462	474	656[b]
M_w/M_n[c]	7.2	3.7	6.0	8.6	5.7	/
M_{max} [kg/mol][d]	16000	2500	11000	27000	21000	/
$Z=M_{max}/M_e$	3000	476	2100	5300	3900	/
XS (%)[e]	3.3	1.9	2.2	1.7	4.8	3.6
η_0 [kPa s][f]	23	1.6	5.5	35	100	170
τ [s][f]	0.79	0.034	0.44	1.6	6.42	10
m	0.71	0.85	0.7	0.7	0.7	0.7
$\tau_{R,max}$ [s][g]	1.39	0.09	0.66	4.14	2.38	/
τ_{term} [s][h]	0.13	0.006[i]	0.019	0.15	0.30	0.59

[a] Weight-average molecular weight (M_w) values for iPP 1-5 are taken from Ref. [5]. [b] The M_w for iPP6 was calculated from the dependence of the zero-shear viscosity, η_0, on M_w (see Equation 5) as in Ref. [15]. [c] M_w/M_n are taken from Ref. [5]. [d] M_{max} represents the high-M_w tail from SEC (see Refs. [5]and [15]). [e] Xylene soluble fraction was taken from Ref. [15] for iPP 1-6, [f] The relaxation time, τ, and the zero-shear viscosity, η_0, were estimated from the fit of the flow curves to the Cross model [15]. [g] $\tau_{R,max}$ is the Rouse time associated with the high-M_w tail $\tau_{R,\max} = \tau_e \left(M_{\max} / M_e \right)^2$ where τ_e is the entanglement strand Rouse time and M_e is the molecular weight of an entanglement strand. Previous work [4,15] fit oscillatory shear data to BoB using the molecular weight distribution and reports $\tau_e = 1.5 \times 10^{-7}$ s at 170 °C and M_e = 5250 g/mol. [h] τ_{term} is the terminal relaxation time estimated as the inverse of the frequency at the dynamic moduli crossover (see Figure S1 in the Supporting Information and Ref. [5]). [i] This value is taken from Ref. [5].

Shear-induced polarized light imaging (SIPLI). Rheo-optical measurements were performed in a Physica MCR 502 (Anton Paar) equipped with a reflection polariscope. This device from Anton Paar is known as Shear-Induced Polarized Light Imaging (SIPLI) [42,43]. The SIPLI setup consists of a

transparent glass bottom plate (viewing window) and an upper 25 mm diameter stainless steel mirror-polished plate which provides the shear flow to the system and reflects the transmitted light. In addition, the polariscope comprises a white light source (SugarCube™), a linear polarizer, a beam splitter, a mirror (in this case the polished surface of the plate), a linear analyzer, a collimating lens (to make the illuminating rays of the light source parallel) and a CCD camera (Lumenera Lu165C color CCD camera) which detects the reflected light. The light is transferred from the light source to the SIPLI setup by means of an optical 6 mm diameter light-guide. The polarization axes of the analyzer and polarizer can be easily regulated from parallel (0°) to orthogonal (90°) for quantitative birefringence measurements under shear. In this work, the SIPLI setup was used for quantifying birefringence under shear and to monitor edge fracture. The temperature was precisely controlled by an electric heater that surrounds the bottom glass plate, in combination with a hood fed with nitrogen gas to minimize sample degradation. The use of a parallel plate for nonlinear shear measurements, although not preferable, has the advantage of accessing various shear rates with one single experiment. Indeed, the actual shear rate at any given radial position r is given by $\dot{\gamma}(r) = \Omega r / h$, where h is the gap height and Ω the angular velocity.

Cone Partitioned Plate (CPP). Shear flow experiments, with minimized edge fracture in the measuring area, were obtained by means of a rotational rheometer equipped with a home-made cone partitioned plate (CPP). This geometry consists of a 6 mm diameter inner plate that is connected to the transducer and a 20 mm corona installed in a hollow bridge connected to the top part of the rheometer which hosts the transducer. The gap between the partitions is around 80 μm. The torque is sensed only by the inner plate. More details on the CPP design, operation and typical uses are reported elsewhere [25,46,47]. We used a strain-controlled ARES-LS rheometer (Rheometrics) equipped with a force rebalance transducer (2KFRTN1). The temperature was controlled by means of an ARES convection oven that can easily accommodate the cone partitioned plate geometry. The oven was fed with a heated stream of nitrogen gas providing an accuracy of ± 0.1 °C. The cone installed in the bottom part of the rheometer (connected to the motor) was a 25 mm diameter stainless steel cone with an angle of 0.05 rad and a truncation gap of 53 μm. Start-up shear experiments were performed at 170 °C (see Figures S7-S11 in the Supporting Information).

Capillary Rheometer. A Rosand dual barrel capillary rheometer (RH10 from Malvern) was used to study the rheology of the iPP samples in Poiseuille flow. Two circular dies of radius 0.5 mm, which have lengths of 10 mm and 0.25 mm for sample pressure and reference pressure, were used in parallel at identical volumetric flow rates. The Bagley correction was taken into account by subtracting the entrance pressure drop from the pressure measured during the test, following Cogswell [48]. More

extended information on flow correction methods are reported elsewhere [49]. Tests were conducted at 170 °C after 10 minutes annealing at 220 °C to load each barrel with bubble-free melt.

RESULTS AND DISCUSSION

Edge Fracture

Figure 2 shows flow curves at 170 °C in parallel plate geometry for three representative polypropylene samples, iPP1, iPP3 and iPP6 (flow curves of the other samples are reported in the next section). Due to the fact that instabilities emerge as the shear rate increases, we refrain from affirming that each data point in Figure 2 represents a steady-state value, especially at high shear rates. In light of this we refer to an "apparent" viscosity. Nevertheless, all the samples enabled estimation of the zero-shear viscosity, given the presence of a clear Newtonian plateau at low shear rates, unaffected by instabilities. In fact, the inset of Figure 2 displays the zero-shear viscosity dependence on M_w for iPP1-5 along with iPP data taken from the literature [50–52] at 170 °C. Such a dependence follows a 3.4 power-law, expected for entangled linear polymer chains in the molten state [53,54]. The following relation was found for the zero-shear viscosity of iPP at 170 ºC with M_w in kg/mol from Table 1:

$$\eta_0 = 4.5\times10^{-5} M_w^{3.4} \quad (\mathrm{Pa\cdot s}) \tag{3}$$

When the shear rate reaches a value in the range 0.5 – 1 s^{-1} a strong shear thinning is detected. For iPP1 and iPP3 the thinning regime is characterized by a slope equal to -1 (see dashed line in Figure 2), a signature of some flow instability. In fact, for the higher M_w iPP6 such a slope is even more pronounced, making the high-shear rate data non-reproducible because of instabilities. Live imaging of the samples under shear identified the cause of this anomalous material response as edge fracture. Figure 3 depicts the procedure we followed to determine the onset shear rate for edge fracture. In particular, Figure 3 shows the flow curve obtained for the iPP1 sample (images for the other samples are reported in Figures S2-S6 in the Supporting Information) in terms of apparent shear viscosity and shear stress, along with birefringence images taken at specific shear rates, corresponding to the solid symbols shown in the flow curve.

At very low shear rates (~10^{-3} s^{-1}), the sample is uniform and evenly distributed in the measuring area. At the shear rates 3.16 s^{-1}, edge fracture commences and it coincides with the decrease in viscosity. Note that the apparent shear thinning of steady state viscosity is significantly enhanced by edge

fracture. Remarkably, at 10 s^{-1}), a substantial amount of the sample was already expelled from the measuring area and the apparent viscosity dropped by one order of magnitude compared to the zero-shear viscosity value. The magnitude of the flow instability increases with the weight-average molecular weight of the sample. It is important to notice that for some systems, as the shear rate increases, a change in the birefringence pattern can be observed, see for instance the iPP1 sample in Figure 3. Stress-induced birefringence can result in a colorful pattern and a few orders of colored fringes may be detected (light retardancy). Isochromatic circular fringes correspond to the lines of constant normal stress differences [43], typical of many polymeric systems [42]. Focusing on iPP1, it is possible to quantify birefringence by using the Michel-Levy chart [55] knowing the light path (twice the measuring gap) and the color (light retardancy). For the two last images of iPP1, the birefringence at the still visible rim of sample takes values of $1.8x10^{-4}$, and $2.5\ x10^{-4}$, the same order of magnitude estimated for polyethylene, another semicrystalline polyolefin [43], above the melting temperature.

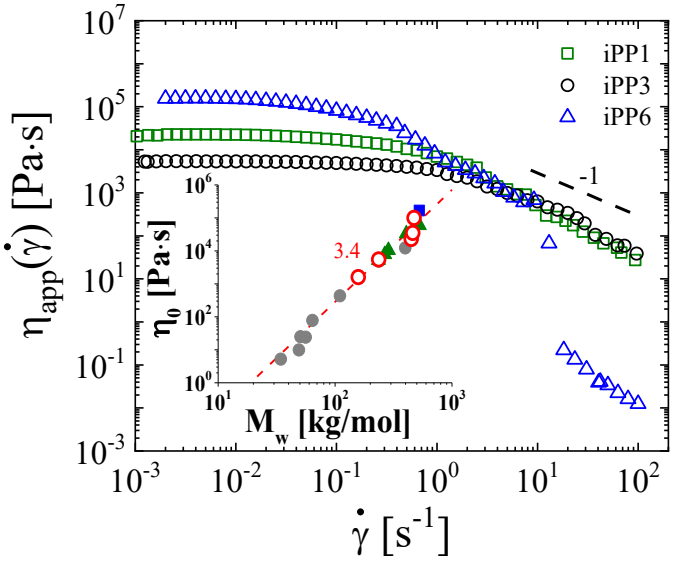

Figure 2. Apparent viscosity as a function of perimeter shear rate for iPP1 (green rectangles), iPP3 (black circles) and iPP6 (blue triangles) samples at 170 °C in parallel plate geometry. Inset: Dependence of the zero-shear viscosity on M_w for iPP1,2,3,4,5 (open red circles), where grey solid circles, blue square and green triangles are taken from literature [50–52].

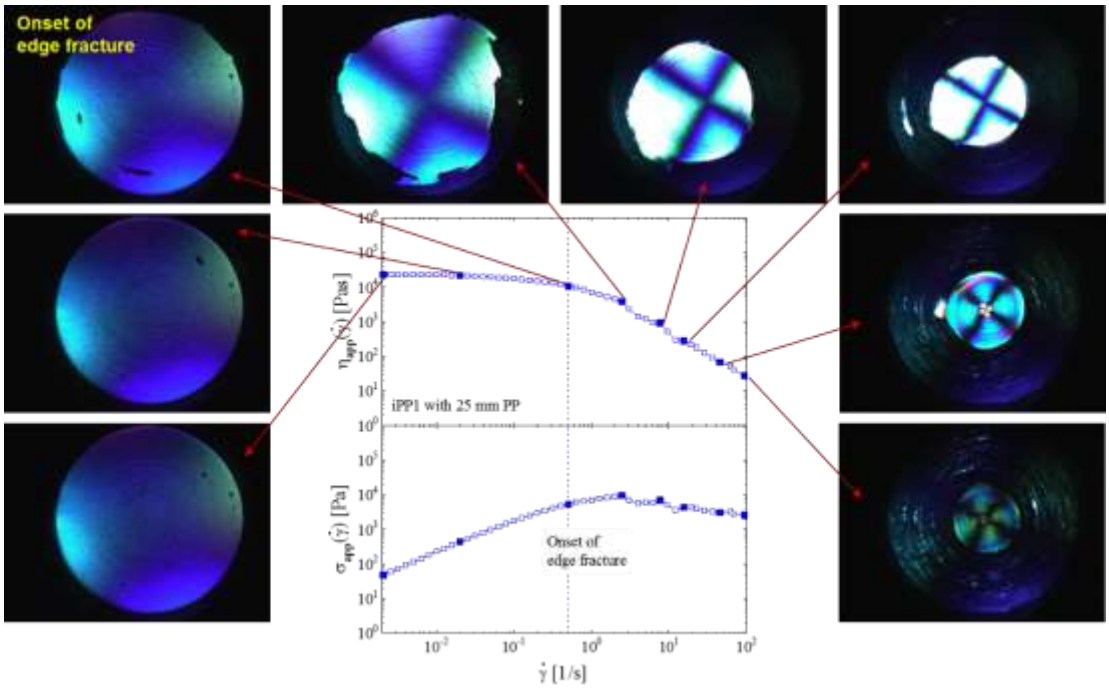

Figure 3. Flow curve in terms of apparent viscosity and shear stress as functions of shear rate at the perimeter of the parallel plates for iPP1 at 170 °C, obtained with 25 mm parallel plates. Birefringent images correspond to the solid symbols in the two plots, as indicated by the red arrows. The perimeter shear rate increases clockwise with the values: 0.002, 0.02, 0.5, 2.5, 7.6, 15.5, 45.3, 93.8 s^{-1}.

Figure 4 displays the shear rate at the onset of edge fracture as a function of the zero-shear viscosity at 170 °C. It was observed that, as the zero-shear viscosity increases, the onset of edge fracture is observed at a lower shear rate. This suggests that the onset of edge fracture can be also predicted for iPP at 170 ºC by knowing the zero-shear viscosity of the sample, which is by far simpler to measure compared to the second normal stress difference N_2. For various measuring systems, Figure 4 reports the onset shear rate for edge fracture $\dot{\gamma}_c$:

$$\dot{\gamma}_c = A\eta_0^{-0.55} \tag{4}$$

with η_0, being the zero-shear viscosity in Pa·s, and A a prefactor that depends on geometry, measuring gap, temperature and material. The prefactor A takes the value of 173, 790, and 62000 at 170 °C for 25 mm, 8 mm parallel plates, and 6 mm CPP, respectively. Poly(ether ether ketone) (PEEK) melts reported in Parisi *et al.* [56,57], as well as some monodisperse linear polystyrene (PS) melts, measured also with a 6 mm CPP, display the same relation between the onset of edge fracture and zero-shear viscosity. Poly(ether ether ketone) refers to 370 ºC, above the nominal melting temperature, with A equal to 9200, whereas polystyrene melts refer to 160 °C, with A equal to 95000. This points to the direction for which the correlation between onset of edge fracture and zero-shear viscosity may prove to be a universal feature of entangled polymers. Note that isotactic polypropylene has a strict linear

chain architecture, whereas poly(ether ether ketone) synthesized by means of polycondensation, may have branches. The measuring gap for parallel plate geometries was set to 1 mm, whereas for the cone-partitioned plate is fixed to the required truncation gap of 0.053 mm. Intuitively, the ratio between the different prefactors reflects the gain in $\dot{\gamma}_c$ when the diameter of the plate is reduced, or the cone-partitioned plate is used. There are three remarks that follow. Once the system, temperature, geometry and gap are chosen, only one experiment is needed; the onset shear rate for edge fracture for another sample can be calculated as $\dot{\gamma}_{c,1} = \dot{\gamma}_{c,2}\left(\frac{\eta_{0,1}}{\eta_{0,2}}\right)^{-0.55}$, with 1 and 2 being two generic samples with different zero-shear viscosity. By combining Eqs. 3 and 4, it is also possible to establish the dependence of the onset shear rate for edge fracture on Mw, $\dot{\gamma}_c \sim M_w^{2.85}$, simplifying further the prediction of edge fracture in any particular geometry at any particular temperature. Quantitative prediction of A is far from trivial. We note in particular the significant difference in the prefactor A between 25 mm parallel plates and 6 mm cone-partitioned plate. Indeed, the reduction of the plate diameter, as well as the measuring gap has a remarkable impact on the onset edge fracture [20, 58] and perhaps even more important is the presence of the partitioned plate, which apparently delays further edge fracture effects in the measuring area.

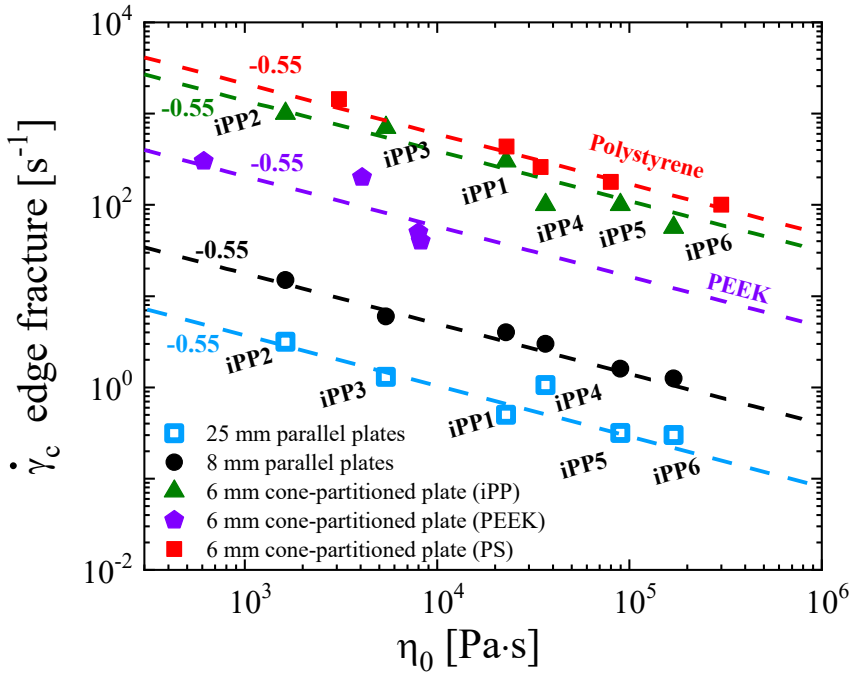

Figure 4. Onset shear rate for edge fracture $\dot{\gamma}_c$ as a function of the zero-shear viscosity η_0 for samples iPP1,2,3,4,5,6 at 170 °C obtained with 25 mm (open blue squares), and 8 mm (filled circles) top

plates, and 50 mm bottom glass plate. Data acquired with a 6 mm cone-partitioned plate (CPP) are reported as filled green triangles. The measuring gap for the parallel plates was 1 mm besides the diameter of the top plate, whereas for the CPP was fixed to 0.053 mm. Data for PEEK melts at 370 ^{o}C from Refs. [56,57], and linear polystyrene melts at 160 ^{o}C are also reported as filled pentagons and squares, respectively. Dashed lines represent Equation 4 with different prefactors discussed in the text.

Shear Rate Dependence of Viscosity and First Normal Stress Difference

Investigating the material response when subjected to strong flow fields is very important for polymer processing and fabrication of polymeric materials, since the final properties and residual stresses are affected by the processing conditions. Flow instabilities often limit the range of shear rates to low values in rotational rheometers (< 1 s^{-1} in the present case). Figure 5 shows flow curves for samples iPP1,2,3,4,5,6 obtained by combining different rheological techniques and instruments. The range of shear rate covers six decades; from the Newtonian plateau to a clear shear thinning regime. Note that, unlike previous works, where flow curves were obtained either by means of time-temperature superposition [59], or capillary rheometry at high temperature [60, 61], the present strategy allows the measurement of flow curves well below the equilibrium melting temperature (~ 187 °C), enabling studies of flow-induced crystallization nearly unaffected by edge fracture. Flow curves are well captured by a phenomenological expression like the Cross model [62]:

$$\eta\left(\dot{\gamma}\right)=\frac{\eta_0}{1+\left(\dot{\gamma}\tau\right)^m} \tag{5}$$

where η_0 is the zero-shear rate viscosity, τ represents the Rouse time of the longest chains in the system [15] and *m* is the shear thinning exponent. The fitting parameters for the Cross model are listed in Table 1. The high quality of the combination of CPP and capillary data is supported by the validity of the empirical Cox-Merz rule [63] for which the steady state viscosity at a given $\dot{\gamma}$ is equal to the complex viscosity at an angular frequency $\omega=\dot{\gamma}$, $\eta\left(\dot{\gamma}\right)=\left|\eta^*\left(\omega\right)\right|$ (see blue dotted lines in Figure 5).

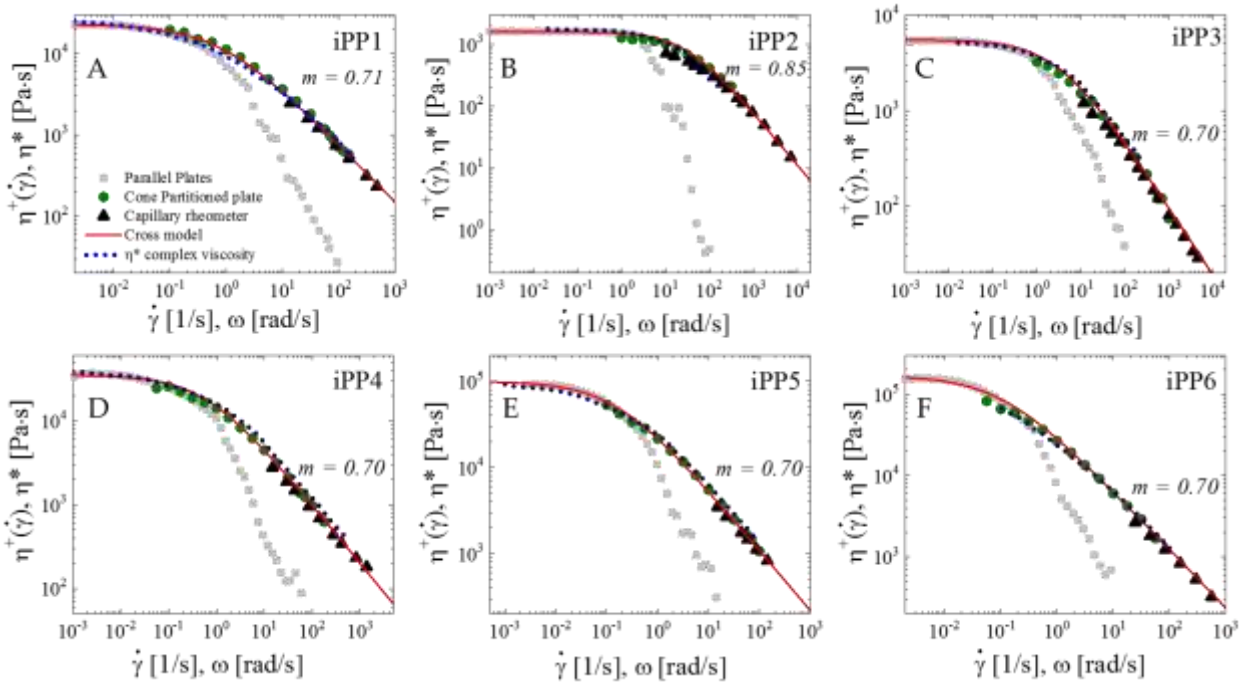

Figure 5. Flow curves for iPP1 (A), iPP2 (B), iPP3 (C), iPP4 (D), iPP5 (E) and iPP6 (F) at 170 °C. The blue dotted lines represent the complex viscosity from linear viscoelastic (LVE) oscillatory shear measurements taken from Ref. [5]. Filled circles and triangles are steady state viscosity data obtained with the CPP and capillary rheometer, respectively, validating the Cox-Merz empirical rule for strictly linear iPPs. Each capillary rheometry data set ends at a shear stress of order 0.1 MPa to avoid shish fomration [15,16]. The red solid lines are fits to the Cross model (Equation 5). Filled squares are 25 mm parallel plate data from a shear rate sweep, which agree with the steady state data at low shear rates but fall strongly below the actual viscosity once edge fracture is severe. The shear thinning exponent *m* is also reported in the Figure for each sample.

Shear thinning commences when polymer chains are oriented and the longest chains start to be stretched in the flow direction. Experiments of nearly monodisperse entangled polymer melts and solutions usually report a shear thinning exponent between 0.8 and 0.9 [22,37,38,39]. Less is known about shear thinning in strictly linear polydisperse entangled polymer melts. Here we report a broad range of iPP samples [59-61,64,65], including those investigated in the present work, each exhibiting shear thinning exponent values between 0.7 and 0.85. Flow curves obtained with parallel plates display an apparent shear thinning exponent much larger than 1, suggesting edge fracture (see the light gray symbols in Figure 5). The shear thinning exponent m of iPP1-5 samples is reported as a function of the polydispersity index in Figure 6A, along with iPP data taken from literature [59-61,64,65]. A decreasing trend with increasing polydispersity is observed when comparing iPP2 with

the others that are more polydisperse, but seems to saturate at a constant value of $m \approx 0.7$ for $5.7 \leq M_w/M_n < 25$. Our tentative hypothesis is that isotropic entangled polydisperse polymer melts with strictly linear chains will never show $m < 0.7$. The same Figure also shows the shear thinning exponent m obtained from the complex viscosity (blue squares in Figure 6A). The high molecular weight samples (iPP5, and iPP6) have enough shear thinning data below 100 rad/s to determine the actual shear thinning exponent (iPP6 is not shown in Figure 6A because M_w/M_n is not known). iPP1,2,3,4 show a significant underestimation of the shear thinning exponent m of Equation 5 based on the complex viscosity. Those lower molecular weight samples simply do not reach the true shear thinning power law in oscillatory shear, which means that the extrapolation of the linear viscoelastic data to estimate viscosity values at high rates, a common practice in industry, *will overestimate the viscosity considerably*! We also note that iPP4 is only 2.6% lower M_w than iPP5 but since iPP4 is far more polydisperse, it still shows this issue.

Figure 6B shows the dependences on the molecular weight of the longest chains [15] M_{max} of (1) τ from the Cross-model fits to Equation 5, (2) the calculated Rouse time of the longest chains [15] $\tau_{R,max,}$ (see Table 1), and (3) the terminal time τ_{term} taken as the reciprocal of the frequency at which G′ and G″ cross (see Figure S1 in the Supporting Information and Ref. [5]). Data for τ taken from the literature [60] are also reported. The calculated Rouse time of the longest chains $\tau_{R,max}$ (see Table 1), displays good agreement with τ estimated from the Cross model, within the error in M_{max} (see horizontal error bars in Figure 6B). This suggests that the onset of shear thinning (τ) is controlled by $\tau_{R,max}$. Consistent with Ref. [15] for a wide range of strictly linear iPP with very different molecular weight distributions [5], the shear thinning onset (τ) is *controlled by stretching the longest chains in the polydisperse molecular weight distribution*; a vital result for future modelling of shear thinning in polydisperse linear polymer melts. Conversely, the terminal time τ_{term} is significantly different from τ, confirming $\tau_{R,max}$ as control parameter for the onset of shear thinning. The power law in Figure 6B with slope of 2 suggests the shortest Rouse time of a Kuhn monomer (with $M_0 = 180$ g/mol) [53] at 170 °C is $\tau_0 = 0.18$ ns and the Rouse time of an entanglement strand (with $M_e = 5250$ g/mol) [5] is 150 ns for iPP at 170 °C .

$$\tau = \tau_{R,\max} = 5 \times 10^{-9} M_{\max}^2 \quad \text{(s)} \tag{6}$$

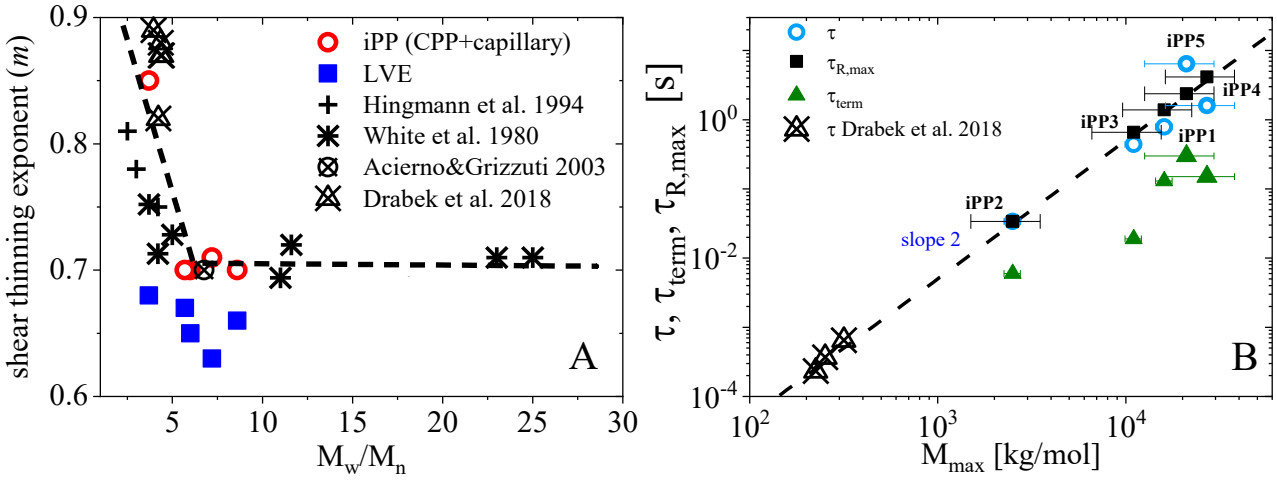

Figure 6. A) Shear thinning exponent dependence on the polydispersity index for iPP1,2,3,4,5 (red circles) at 170 °C. The dashed black line is a guide for the eye. Blue solid squares are the shear thinning exponent estimated by considering the steepest slope of the complex viscosity curve at 170 °C and these are invariably lower than the actual power law exponent for viscosity when the latter includes data at high shear rates, because the frequency is not high enough to reach the true power law exponent. iPP2 has the narrowest chain length distribution and the industry ploy of extrapolating the power law part of the Cross model fit of complex viscosity to high shear rates fails miserably. Literature data [59-61,64,65] are also shown (see Figure legend). B) Longest relaxation time for iPP1,2,3,4,5 obtained from the fit of the viscosity data to the Cross model (circles), the terminal time τ_{term} (triangles) taken as the reciprocal of the frequency at which G′ and G″ cross (see Figure S1 in the Supporting Information and Ref. [5]), and the calculated $\tau_{R,max}$ (see Table 1) at 170 °C, as functions of the molecular weight of the longest chains M_{max}. Data from Ref. [60] are also reported (see Figure legend). Stretching the longest chains in the distribution seems to control the shear thinning onset. The dashed line in panel B has a slope of 2, capturing the trend of the characteristic time obtained from the Cross model fit. Horizontal error bars are calculated from the molecular weight distributions reported in Ref. [5].

To further highlight the shear thinning region, we combined the main results of Figures 5 and 6A into Figure 7. Here we report the flow curves for all six samples, considering only the data obtained with the CPP (open symbols), and capillary rheometry (solid symbols). The linear viscoelastic response is also reported (solid lines). A good overlap between CPP and capillary rheometry was always observed. A slight difference observed at 10 s^{-1} for the iPP2 sample is due to the pressure signal approaching the minimum resolution of the transducer for our capillary rheometer. The maximum shear rate attained with the capillary rheometer was limited by the maximum shear stress above which shish structures can be formed [15]. Whereas this aspect is certainly intriguing for further FIC studies,

here we focused on flow curves with well-resolved shear thinning regime, unaffected by either flow instabilities or structural changes promoted by the shear flow. As presented in Figure 6A, all the iPP samples with polydispersity larger than 5 exhibit a shear thinning exponent equal to 0.7. Remarkably, the inset of Figure 7 shows that, when the consistency index from Eq. 5, $\eta_0\tau^{-0.7}$, is plotted against Mw, our data along with other iPPs taken from the literature [59,65] display a linear trend (with $\eta_0 \sim M_w^{3.4}$ and $\tau \sim M_w^{3.4}$ the exponent for the consistency index should be 3.4(0.3) = 1). Such a result provides the unique correlation between the shear thinning of polydisperse entangled strictly linear polymer chains with their weight-average molecular weight.

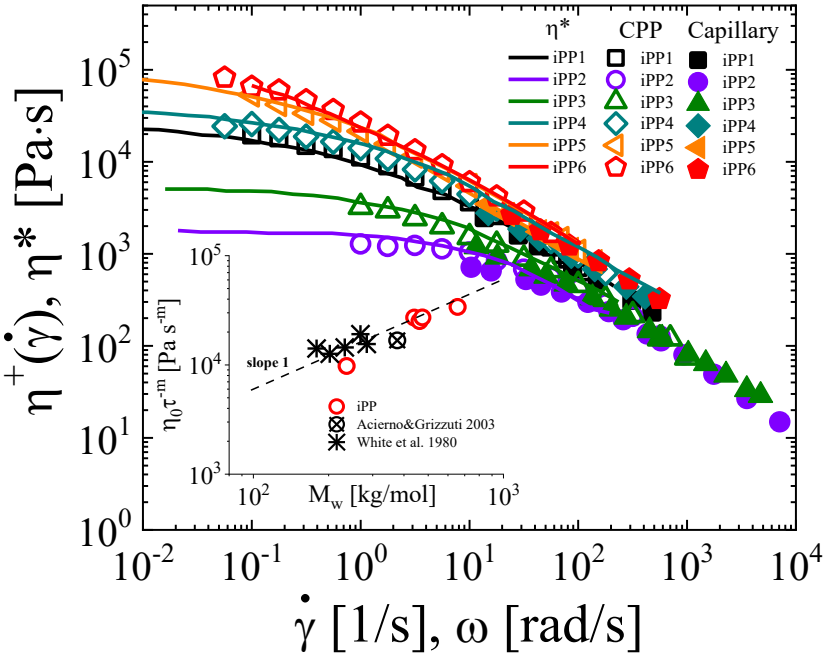

Figure 7. Flow curves for iPP1 (squares), iPP2 (circles), iPP3 (up-pointed triangles), iPP4 (diamonds), iPP5 (left-pointed triangles) and iPP6 (pentagons) at 170 °C. Capillary data are shown as solid symbols, whereas cone-partitioned plate (CPP) data are shown as open symbols. Solid lines represent the complex viscosity from linear viscoelastic (LVE) oscillatory shear measurements taken from Ref. [5]. Inset: consistency index as a function of Mw for iPP1,3,4,5,6 along with data taken from the literature [59,65], all exhibiting a shear thinning exponent equal to 0.7. The black dashed line has a slope equal to one.

Figure 8 shows the start-up of shear experiments for iPP4 in terms of the growth of shear stress σ^+ (panel A) and first normal stress difference N_1^+ (panel B) as functions of time at various shear rates. Experiments were performed with a 6 mm cone partitioned plate (CPP) to avoid edge fracture effects.

The minimum shear rate was dictated by the minimum torque resolution of the instrument, whereas the maximum shear rate was bound by either edge fracture, that eventually reaches the measuring area, or the maximum normal force allowed by the transducer (29 N or ~ 1 MPa as a largest measurable normal stress with a 6 mm CPP). Note that the range of shear rates for N_1^+ is narrower than for the shear stress, as the normal force signal was either significantly noisy at low shear rates or "saturated" at high shear rates because of the maximum normal force measurable by the transducer. Note that the increase in both shear stress growth σ^+ and first normal stress difference growth N_1^+ at shear rates 70 and 100 s^{-1} is caused by overcoming the shear stress threshold value of 0.1 MPa to form shish in iPP [15,16]. Start-up of shear experiments for the other iPP samples are reported in Figures S7-S11 in the Supporting Information.

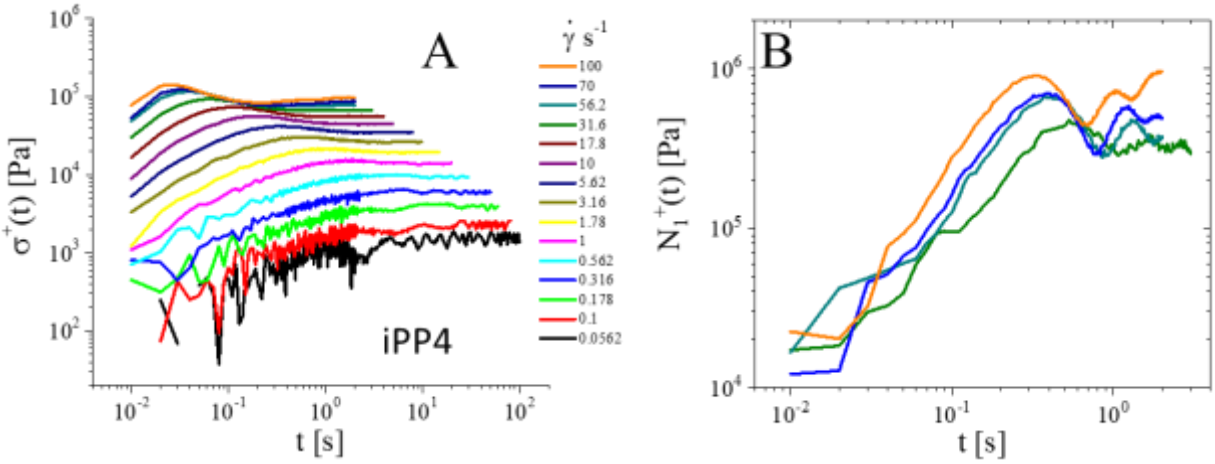

Figure 8. Start-up of shear in terms of shear stress growth σ^+ (panel A) and first normal stress difference growth N_1^+ (panel B) as a function of time at various shear rates (reported in the figure) for iPP4 at 170 °C, obtained with the 6 mm cone partitioned plate at 170 °C. Note that the increase in both shear stress growth σ^+ and first normal stress difference growth N_1^+ at shear rates 70 and 100 s^{-1} is caused by exceeding the shear stress threshold value 0.1 MPa to form shish [15,16].

The steady-state value of the apparent first normal stress difference N_1 for iPP1,2,3,4,5 as a function of Weissenberg number $\dot{\gamma}\tau$ that is the product of shear rate and the Cross model relaxation time τ, is shown in Figure 8A. This plot reduces all data and displays a power law shear rate dependence with exponent 0.5 (shown as the dashed line in Figure 9A) as typically seen in entangled polymer melts at shear rates much higher than $1/\tau$ [49,66]. The steady-state values of N_1 are validated by the linear viscoelastic data through Laun's empirical relation (see Figure S12 in the Supporting Information) [67,68]. Note that, all the iPP samples fall into a master curve, suggesting that the dynamics are

controlled by the stretching of the longest chains. Figure 9B shows the dependence of the same steady-state values of the apparent first normal stress difference N_1 on the steady-state values of the shear stress σ. Such a representation was first reported by White *et al*. on polystyrene melts [69,70], with the aim of determining normal stresses in melts without having to directly measuring them. The N_1/σ ratio may be interpreted as the ratio of the energy stored to the energy dissipated by the system, similar to the ratio between the storage modulus G′ and the loss modulus G″ [71]. White *et al*. demonstrated that the correlation between N_1 and σ is independent of temperature but dependent upon the molecular weight distribution, reporting $N_1 \sim \sigma^{1.66}$ for a broad collection of data on polymer melts and $N_1 \sim \sigma^{2.0}$ for nearly monodisperse polystyrenes. Han and Jhon [71] as well as Kitano *et al*. [72] found $N_1 \sim \sigma^{2.0}$ in polyethylene melts. In the present case, we found a $N_1 \sim \sigma^{1.66}$ dependence for iPP1,2,3,4,5 within the error in estimating the steady state value of N_1 (see Figures S7-S11 in the Supporting Information). The range of shear rates reported in Figure 7 refers to the shear thinning regime, where $N_1 \sim \dot{\gamma}^{1/2}$ (see Figure 7A), $\sigma \sim \dot{\gamma}^{0.3}$ (assuming a shear thinning exponent m = 0.70), therefore, $N_1 \sim \sigma^{1.66}$. Indeed, a weaker dependence can be observed for iPP2. The iPP2 sample represents not only the sample with the smallest polydispersity, but also that with the smallest M_w (see Table 1). This means that the shear thinning is reached at much larger rates compared to other iPPs investigated in this work. To this end, Figure 5B shows that the thinning regime is well captured by capillary data, whereas N_1 was measured with the CPP, therefore, at lower rates. If we use the shear thinning exponent estimated from the CPP data (underestimated) we obtain m = 0.6, which translates into $N_1 \sim \sigma^{1.25}$. The latter dependence, within errors, is in good agreement with the trend displayed by the iPP2 sample in Figure 8B. It is also worth mentioning that some of the polystyrenes studied by Oda *et al*. [60] with M_w/M_n = 18 displayed steeper slopes, suggesting that the stronger N_1 dependence on σ may be due to polydispersity, as also observed in extrudate swell experiments with slit dies by Graessley, Glasscock and Crawley [73].

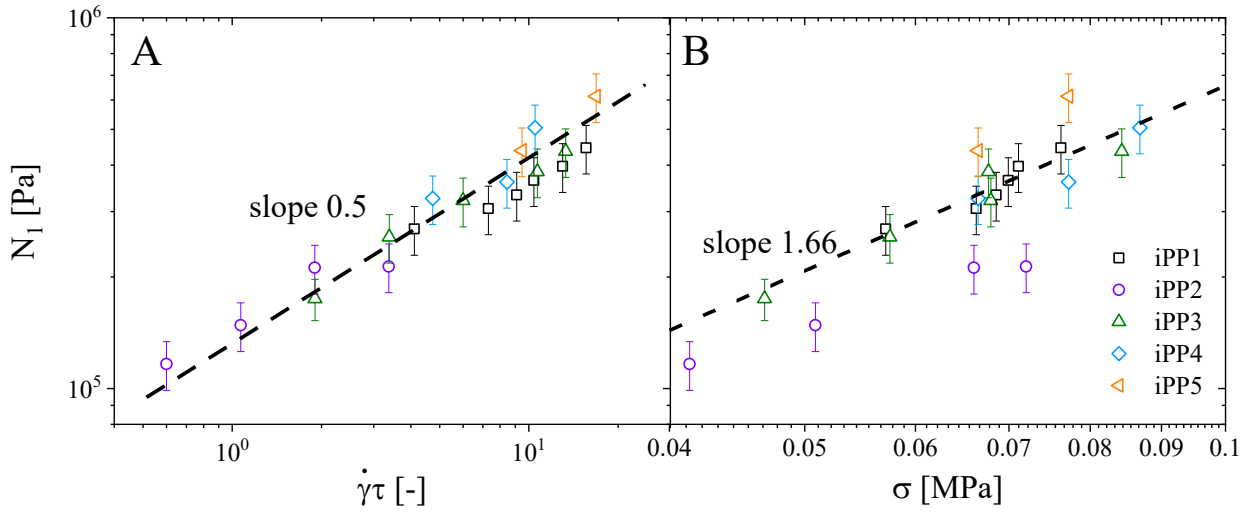

Figure 9. Steady-state first normal stress difference N_1 as a function of A) Weissenberg number that is the shear rate normalized by the Cross model relaxation time τ (listed in Table 1) and B) steady-state shear stress at 170 °C, for iPP1 (black squares), iPP2 (purple circles), iPP3 (green up-pointing triangles), iPP4 (cyan diamonds) and iPP5 (orange left-pointing triangles). N_1 curves are reported in B panels of Figures 7 and S7-S11. Error bars are obtained by averaging at least 20 data points in the steady-state. Error bars for the steady-state stress are within the size of the symbols. Experiments were performed with a 6 mm cone partitioned plate at 170 °C.

Note that iPP6 is not shown in Figure 9 because either the normal force signal was too weak to resolve or the shear stress magnitude was high enough to promote the formation of a large fraction of FIC precursors, as shown and discussed by Nazari *et al*. [15]. Lastly, we contrasted the N_2 values inferred from the N_1 data reported in Figure 8B with Eq.2, by $-N_2/N_1 = 0.1$ based on the probed range of shear rates [25], a surface tension Γ equal to 0.032 N/m [74], and a gap of 53 μm. Considering the highest stress reported in Figure 8B (~ 0.085 MPa), we obtained $N_{2c} = 38000$ Pa, which is always larger than any $0.1N_1$ data in Figure 9B, excepts for the iPP5 sample. However, the difference is about 20%, considered still reasonable given the crude calculation.

CONCLUSIONS

The onset shear rate $\dot{\gamma}_c$ for edge fracture follows a decreasing power-law trend as the zero-shear viscosity of the polymer increases, with $\dot{\gamma}_c = A\eta_0^{-0.55}$. A is a prefactor which depends on temperature, measuring system, gap and material investigated. This empirical correlation lays the foundation for a more general prediction of edge fracture of polymers from the zero-shear viscosity, which is far

simpler to measure compared to the second normal stress difference. Although this seems of general validity due to the strict linear chain structure of isotactic polypropylene, whether or not such a simple correlation applies to other polymers (linear chains with different polydispersities and long chain branched polymers) is a great topic for future research.

Once identified, edge fracture can be significantly suppressed at a temperature below the equilibrium melting temperature by using a cone partitioned plate. When complemented by capillary rheometry, this enables the measurements of quite extended flow curves, with well resolved shear thinning. The shear thinning exponent for a large number of iPP was found to decrease from ~0.85 to a plateau value of 0.7 with increasing polydispersity. This rheometer combination can be exploited to enable a thorough investigation of the shear thinning steady state viscosity of all thermoplastic polymers, as well as studying flow-induced crystallization unaffected by edge fracture.

The onset of the shear viscosity thinning is controlled by the Rouse relaxation time of the longest chains in the system, rather than the terminal time, which for these polydisperse melts is considerably shorter. This represents a crucial result for modelling the shear thinning of polydisperse linear polymer melts.

Lastly, the relation between first normal stress difference and shear stress, $N_1 \sim \sigma^{1.66}$, enables the possibility to estimate normal stress by simply measuring shear stress, a quantity which is much simpler to measure, especially in commercially available rotational rheometers that have surprisingly low limits for the largest values of normal force. Modern rotational rheometers have a very sensitive transducer for measuring normal force but cannot measure normal stresses at the high shear rates relevant to many polymer processing operations.

SUPPORTING INFORMATION

Small amplitude oscillatory shear at 170 °C; Flow curves and birefringent images at 170°C; Start-up of shear in terms of shear stress growth σ^+ and first normal stress difference growth N_1^+ as a function of time at various shear rates at 170 °C; Comparison between steady-state values of N_1^+ and the empirical prediction proposed by Laun.

AUTHOR INFORMATION

Corresponding Author

*Ralph H. Colby

E-mail rhc@plmsc.psu.edu

Tel +1-814-863-3457

ORCID

Daniele Parisi http://orcid.org/0000-0002-1650-8429

Aijie Han https://orcid.org/0000-0002-9309-5912

Jiho Seo https://orcid.org/0000-0001-9374-4591

Ralph H. Colby https://orcid.org/0000-0002-5492-6189

ACKNOWLEDGMENTS

We gratefully acknowledge the National Science Foundation, Division of Materials Research, Polymers Program for funding under DMR-1807934. The authors would like to thank Prof. Dimitris Vlassopoulos (University of Crete – IESL FORTH) for providing the polystyrene data in Figure 4. The authors also thank Abhijeet Maniktala for help with some rheological experiments and Doug Harrell of the Phillips 66 Company for providing the sample iPP6.

References

[1] Housmans J-W, Steenbakkers RJ, Roozemond PC, Peters GW, Meijer HE. Saturation of pointlike nuclei and the transition to oriented structures in flow-induced crystallization of isotactic polypropylene. Macromolecules 2009;42:5728–5740.

[2] Elmoumni A, Winter HH, Waddon AJ, Fruitwala H. Correlation of material and processing time scales with structure development in isotactic polypropylene crystallization. Macromolecules 2003;36:6453–6461.

[3] Kumaraswamy G, Issaian AM, Kornfield JA. Shear-enhanced crystallization in isotactic polypropylene. 1. Correspondence between in situ rheo-optics and ex situ structure determination. Macromolecules 1999;32:7537–7547.

[4] Hamad FG, Colby RH, Milner ST. Lifetime of flow-induced precursors in isotactic polypropylene. Macromolecules 2015;48:7286–7299.

[5] Hamad FG, Colby RH, Milner ST. Onset of flow-induced crystallization kinetics of highly isotactic polypropylene. Macromolecules 2015;48:3725–3738.

[6] Zhou Y-G, Turng L-S, Shen C-Y. Morphological evolution and orientation development of stretched iPP films: Influence of draw ratio. Journal of Polymer Science Part B: Polymer Physics 2010;48:1223–1234.

[7] Zhang C, Hu H, Wang X, Yao Y, Dong X, Wang D, Whang Z., Han CC. Formation of cylindrite structures in shear-induced crystallization of isotactic polypropylene at low shear rate. Polymer 2007;48:1105–1115.

[8] Varga J. Characteristics of cylindritic crystallization of polypropylene. Die Angewandte Makromolekulare Chemie: Applied Macromolecular Chemistry and Physics 1983;112:191–203.

[9] Varga J, Karger-Kocsis J. Rules of supermolecular structure formation in sheared isotactic polypropylene melts. Journal of Polymer Science Part B: Polymer Physics 1996;34:657–670.

[10] Azzurri F, Alfonso GC. Insights into formation and relaxation of shear-induced nucleation precursors in isotactic polystyrene. Macromolecules 2008;41:1377–1383.

[11] Cavallo D, Azzurri F, Balzano L, Funari SS, Alfonso GC. Flow memory and stability of shear-induced nucleation precursors in isotactic polypropylene. Macromolecules 2010;43:9394–9400.

[12] Hamad FG, Colby RH, Milner ST. Transition in crystal morphology for flow-induced crystallization of isotactic polypropylene. Macromolecules 2016;49:5561–5575.

[13] Nogales A, Hsiao BS, Somani RH, Srinivas S, Tsou AH, Balta-Calleja FJ, Ezquerra TA. Shear-induced crystallization of isotactic polypropylene with different molecular weight distributions: in situ small-and wide-angle X-ray scattering studies. Polymer 2001;42:5247–5256.

[14] Somani RH, Hsiao BS, Nogales A, Srinivas S, Tsou AH, Sics I, Balta-Calleja FJ, Ezquerra TA. Structure development during shear flow-induced crystallization of i-PP: in-situ small-angle X-ray scattering study. Macromolecules 2000;33:9385–9394.

[15] Nazari B, Tran H, Beauregard B, Flynn-Hepford M, Harrell D, Milner ST, Colby RH. Two distinct morphologies for semicrystalline isotactic polypropylene crystallized after shear flow. Macromolecules 2018;51:4750–4761.

[16] Balzano L, Ma Z, Cavallo D, van Erp TB, Fernandez-Ballester L, Peters GW. Molecular aspects of the formation of shish-kebab in isotactic polypropylene. Macromolecules 2016;49:3799–3809.

[17] Tanner RI, Keentok M. Shear fracture in cone-plate rheometry. Journal of Rheology 1983;27:47–57.

[18] Hemingway EJ, Fielding SM. Edge fracture instability in sheared complex fluids: Onset criterion and possible mitigation strategy. Journal of Rheology 2019;63:735–750.

[19] Larson RG. Instabilities in viscoelastic flows. Rheologica Acta 1992;31:213–263.

[20] Keentok M, Xue S-C. Edge fracture in cone-plate and parallel plate flows. Rheologica Acta 1999;38:321–348.

[21] Hutton JF. Fracture of liquids in shear. Nature 1963;200:646–648.

[22] Costanzo S, Huang Q, Ianniruberto G, Marrucci G, Hassager O, Vlassopoulos D. Shear and extensional rheology of polystyrene melts and solutions with the same number of entanglements. Macromolecules 2016;49:3925–3935.

[23] Schweizer T. Measurement of the first and second normal stress differences in a polystyrene melt with a cone and partitioned plate tool. Rheologica Acta 2002;41:337–344.

[24] Snijkers F, Vlassopoulos D. Cone-partitioned-plate geometry for the ARES rheometer with temperature control. Journal of Rheology 2011;55:1167–1186.

[25] Costanzo S, Ianniruberto G, Marrucci G, Vlassopoulos D. Measuring and assessing first and second normal stress differences of polymeric fluids with a modular cone-partitioned plate geometry. Rheologica Acta 2018;57:363–376.

[26] Mall-Gleissle SE, Gleissle W, McKinley GH, Buggisch H. The normal stress behaviour of suspensions with viscoelastic matrix fluids. Rheologica Acta 2002;41:61–76.

[27] Mykhaylyk OO, Chambon P, Impradice C, Fairclough JPA, Terrill NJ, Ryan AJ. Control of structural morphology in shear-induced crystallization of polymers. Macromolecules 2010;43:2389–2405.

[28] Cwalina CD, Wagner NJ. Material properties of the shear-thickened state in concentrated near hard-sphere colloidal dispersions. Journal of Rheology 2014;58:949–67.

[29] Jeong S, Kim JM, Baig C. Effect of chain orientation and stretch on the stress overshoot of entangled polymeric materials under start-up shear. Macromolecules 2017;50:3424–3429.

[30] Doi M, Edwards SF. The theory of polymer dynamics. Oxford: Clarendon Press; 1988.

[31] Marrucci G. Fast flows of concentrated polymers: predictions of the tube model on chain stretching. Gazz. Chim. Itali. 1988;118:179–185.

[32] Pearson D, Herbolzheimer E, Grizzuti N, Marrucci G. Transient behavior of entangled polymers at high shear rates. Journal of Polymer Science Part B: Polymer Physics 1991;29:1589–1597.

[33] Marrucci G. Dynamics of entanglements: A nonlinear model consistent with the Cox-Merz rule. Journal of Non-Newtonian Fluid Mechanics 1996;62:279–289.

[34] Ianniruberto G, Marrucci G. On compatibility of the Cox-Merz rule with the model of Doi and Edwards. Journal of Non-Newtonian Fluid Mechanics 1996;65:241–6.

[35] Ianniruberto G, Marrucci G. Convective constraint release (CCR) revisited. Journal of Rheology 2014;58:89–102.

[36] Ianniruberto G. Quantitative appraisal of a new CCR model for entangled linear polymers. Journal of Rheology 2015;59:211–235.

[37] Wang S-Q. Nonlinear polymer rheology. Wiley Online Library; 2018.

[38] Graessley WW. The entanglement concept in polymer rheology. The Entanglement Concept in Polymer Rheology, Berlin/Heidelberg: Springer-Verlag; 1974, p. 1–179.

[39] Parisi D, Costanzo S, Jeong Y, Ahn J, Chang T, Vlassopoulos D, Halverson JD, Kremer K, Ge T, Rubinstein M, Grest GS, Srinin W, Grosberg AY. Nonlinear Shear Rheology of Entangled Polymer Rings. Macromolecules 2021. **DOI:** 10.1021/acs.macromol.0c02839

[40] Milner ST. Relating the shear-thinning curve to the molecular weight distribution in linear polymer melts. Journal of Rheology 1996;40:303–315.

[41] Nichetti D, Manas-Zloczower I. Viscosity model for polydisperse polymer melts. Journal of Rheology 1998;42:951–969.

[42] Mykhaylyk OO, Warren NJ, Parnell AJ, Pfeifer G, Laeuger J. Applications of shear-induced polarized light imaging (SIPLI) technique for mechano-optical rheology of polymers and soft matter materials. Journal of Polymer Science Part B: Polymer Physics 2016;54:2151–2170.

[43] Mykhaylyk OO. Time-resolved polarized light imaging of sheared materials: application to polymer crystallization. Soft Matter 2010;6:4430–4440.

[44] Iijima M, Strobl G. Isothermal crystallization and melting of isotactic polypropylene analyzed by time-and temperature-dependent small-angle X-ray scattering experiments. Macromolecules 2000;33:5204–5214.

[45] Sadiku ER. Thermal studies on isotactic polypropylene. Measurements of Tg, Tm and ΔHf. Acta Polymerica 1990;41:246–51.

[46] Yan Z-C, Costanzo S, Jeong Y, Chang T, Vlassopoulos D. Linear and nonlinear shear rheology of a marginally entangled ring polymer. Macromolecules 2016;49:1444–1453.

[47] Parisi D, Seo J, Nazari B, Schaake RP, Rhoades AM, Colby RH. Shear-Induced Isotropic–Nematic Transition in Poly (ether ether ketone) Melts. ACS Macro Letters 2020;9:950–956.

[48] Cogswell FN. Polymer melt rheology: a guide for industrial practice. Elsevier; 1981.

[49] Macosko, C. W. Rheology: Principles, Measurements and Applications (1994) VCH, New York.

[50] Eckstein A, Friedrich C, Lobbrecht A, Spitz R, Mülhaupt R. Comparison of the viscoelastic properties of syndio-and isotactic polypropylenes. Acta Polymerica 1997;48:41–46.

[51] Alle N, Lyngaae-Jørgensen J. Polypropylene and polyethylene blends. Rheologica Acta 1980;19:94–103.

[52] Ouano AC, Mercier PL. The molecular weight distribution of polypropylene. Journal of Polymer Science Part C: Polymer Symposia, Wiley Online Library; 1968, p. 309–315.

[53] Rubinstein M, Colby RH. Polymer physics. Oxford University Press New York; 2003.

[54] Berry GC, Fox TG. The viscosity of polymers and their concentrated solutions. Fortschritte der Hochpolymeren-Forschung, Springer; 1968, p. 261–357.

[55] Bloss FD. Optical Crystallography. Chantilly VA: Mineralogical Society of America; 1999. 239pp.

[56] Parisi D, Seo J, Schaake RP, Rhoades AM, Colby RH. Shear-induced nematic phase in entangled rod-like PEEK melts. Progress in Polymer Science 2021;112:101323.

[57] Parisi D, Seo J, Nazari B, Schaake RP, Rhoades AM, Colby RH. Shear-Induced Isotropic–Nematic Transition in Poly (ether ether ketone) Melts. ACS Macro Letters 2020;9:950–956.

[58] Howells ER., Benbow JJ. Flow defects in polymer melts. Trans. Plast. Inst. 30 (1962): 240-253.

[59] Acierno S, Grizzuti N. Measurements of the Rheological Behavior of a Crystallizing Polymer by an “Inverse Quenching” Technique. Journal of Rheology 47.2 2003:563-573.

[60] Drabek J, Zatloukal M., Martyn M. Effect of Molecular Weight on Secondary Newtonian Plateau at High Shear Rates for Linear Isotactic Melt Blown Polypropylenes. Journal of Non-Newtonian Fluid Mechanics 251 2018:107-118.

[61] Drabek J, Zatloukal M., Martyn M. Effect of Molecular Weight, Branching and Temperature on Dynamics of Polypropylenes Melts at Very High Shear Rates. Polymer 144 2018: 179-183.

[62] Cross MM. Rheology of non-Newtonian fluids: a new flow equation for pseudoplastic systems. Journal of Colloid Science 1965;20:417–437.

[63] Cox WP, Merz EH. Correlation of dynamic and steady flow viscosities. Journal of Polymer Science 1958;28:619–622.

[64] Hingmann R, Marczinke BL. Shear and Elongational Flow Properties of Polypropylenes Melts. Journal of Rheology 38, 573 1994: 573-587.

[65] Wataru M, White JL, Spruiell JE. Experimental Investigation of the Influence of Molecular Weigth Distribution on the Rheological Properties of Polypropylene Melts. Polymer Engineering and Science 20 17 1980: 1166-1176.

[66] Baird DG. First normal stress difference measurements for polymer melts at high shear rates in a slit-die using hole and exit pressure data. Journal of Non-Newtonian Fluid Mechanics 2008;148:13–23.

[67] Laun, H. M., Prediction of Elastic Strains of Polymer Melts in Shear and Elongation. Journal of Rheology 1986;30:459–501.

[68] Sharma, V., and G. H. McKinley, An Intriguing Empirical Rule for Computing the First Normal Stress Difference From Steady Shear Viscosity Data for Concentrated Polymer Solutions and Melts, Rheologica Acta 2012;51:487–95.

[69] Oda K, White JL, Clark ES. Correlation of normal stresses in polystyrene melts and its implications. Polymer Engineering & Science 1978;18:25–28.

[70] Lobe VM, White JL. An experimental study of the influence of carbon black on the rheological properties of a polystyrene melt. Polymer Engineering & Science 1979;19:617–624.

[71] Han CD, Jhon MS. Correlations of the first normal stress difference with shear stress and of the storage modulus with loss modulus for homopolymers. Journal of Applied Polymer Science 1986;32:3809–3840.

[72] Kitano T, Kataoka T, Nagatsuka Y. Shear flow rheological properties of vinylon-and glass-fiber reinforced polyethylene melts. Rheologica Acta 1984;23:20–30.

[73] Graessley WW, Glasscock SD, Crawley RL. Die swell in molten polymers. Transactions of the Society of Rheology 1970;14:519–544.

[74] Burrel H, Immergut B. Polymer Handbook 2nd. edn., Wiley-Interscience, New York, NY, 1975:221-228